

Elucidating the Inter-system Crossing of the Nitrogen-Vacancy Center up to Megabar Pressures

Benchen Huang,^{1,*} Srinivas V. Mandyam,^{2,*} Weijie Wu,² Bryce Kobrin,^{3,4} Prabudhya Bhattacharyya,^{3,4} Yu Jin,⁵ Bijuan Chen,² Max Block,² Esther Wang,⁶ Zhipan Wang,² Satcher Hsieh,^{3,4} Chong Zu,⁷ Christopher R. Laumann,⁸ Norman Y. Yao,^{2,3,4,†} and Giulia Galli^{1,5,9,‡}

¹*Department of Chemistry, University of Chicago, Chicago, IL 60637, USA*

²*Department of Physics, Harvard University, Cambridge, MA 02135, USA*

³*Department of Physics, University of California, Berkeley, CA 94720, USA*

⁴*Materials Science Division, Lawrence Berkeley National Laboratory, Berkeley, CA 94720, USA*

⁵*Pritzker School of Molecular Engineering, University of Chicago, Chicago, IL 60637, USA*

⁶*Department of Chemistry and Chemical Biology, Harvard University, Cambridge, MA 02135, USA*

⁷*Department of Physics, Washington University, St. Louis, MO 63130, USA*

⁸*Department of Physics, Boston University, Boston, MA 02215, USA*

⁹*Materials Science Division and Center for Molecular Engineering, Argonne National Laboratory, Lemont, IL 60439, USA*

(Dated: March 3, 2026)

The integration of Nitrogen-Vacancy color centers into diamond anvil cells has opened the door to quantum sensing at megabar pressures. Despite a multitude of experimental demonstrations and applications ranging from quantum materials to geophysics, a detailed microscopic understanding of how stress affects the NV center remains lacking. In this work, using a combination of first principles calculations as well as high-pressure NV experiments, we develop a complete description of the NV's optical properties under general stress conditions. In particular, our *ab initio* calculations reveal the complex behavior of the NV's inter-system crossing rates under stresses that both preserve and break the defect's symmetry. Crucially, our proposed framework immediately resolves a number of open questions in the field, including: (i) the microscopic origin of the observed contrast-enhancement in (111)-oriented anvils, and (ii) the surprising observation of NV contrast-inversion in certain high-pressure regimes. Our work lays the foundation for optimizing the performance of NV high-pressure sensors by controlling the local stress environment, and more generally, suggests that symmetry-breaking stresses can be utilized as a novel tuning knob for generic solid-state spin defects.

Pressure represents a powerful tuning knob for condensed matter systems, enabling access to novel physical states, ranging from record-high temperature superconductivity [1] to exotic structural phases [2]. Access to megabar pressures [3] in the laboratory is enabled by the diamond anvil cell (DAC) [Fig. 1(a)], an apparatus consisting of two opposing diamond tips that compress a small sample within a gasketed chamber. However, the DAC imposes severe constraints on metrology. Perhaps the most important is the inability to perform spatially-resolved local measurements of the physics inside the high-pressure chamber [4–6].

To this end, a tremendous amount of excitement has centered on the integration of nitrogen vacancy (NV) color centers into diamond anvil cells [7–15]. By directly implanting such spin-defect sensors into the anvil tip (i.e. culet) applying the pressure [7–9], seminal recent experiments have demonstrated the ability to image local stresses and magnetism with sub-micron resolution [16]. This approach has had an almost immediate impact on our understanding of multiple families of materials under pressure, ranging from hydride [12, 17, 18] and nickelate [19, 20] superconductors to magnetic min-

erals [13]. It is now possible to resolve sub-micron scale heterogeneities in functional materials at high pressure, and to correlate them with their structural and stoichiometric sources [19].

Despite these successes, our microscopic understanding of the NV center under pressure remains relatively nascent, with two broad sets of open questions. First, it is generally believed that the stress environment must be carefully managed in order to enable high-pressure NV quantum sensing [Fig. 1(b)] [21–24]. As an example, the NV's optical contrast depends sensitively on its crystallographic orientation relative to the culet [12–14]. However, the underlying reasons for this sensitivity—and whether more optimal stress conditions exist—remain unclear. Second, a multitude of experiments across a variety of conditions [11, 12], have all observed the puzzling *inversion* of NV contrast under pressure [Fig. 1(c)] [12]. On one hand, this inversion complicates signal extraction from the NV center; on the other, it may offer metrological advantages of its own. Taken together, these questions point to the importance of developing a microscopic framework for understanding and predicting the properties of NV centers in a generic

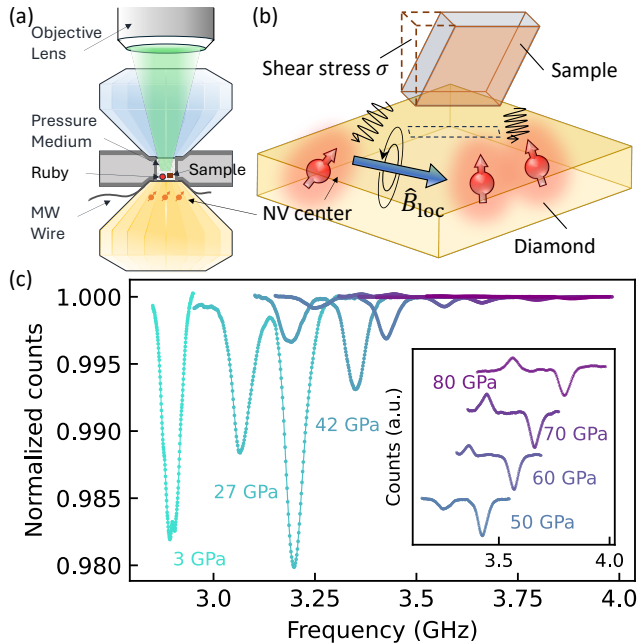


Figure 1. (a) Schematic of the diamond anvil cell (DAC) geometry. The DAC sample chamber is defined by the gasket-anvil assembly; it is loaded with the sample of interest, pressure-transmitting medium, and a ruby microsphere. A ~ 50 -nm layer of NV centers (about 1 ppm density) is embedded into the diamond anvil directly below the sample chamber. For ODMR measurements, a platinum wire is placed on the bottom culet to deliver microwaves. (b) Major quantum sensing applications using the NV center include magnetometry [25] and sensing normal and shear (depicted) stresses σ in the sample [26–29]. (c) Continuous-wave ODMR measurements of NV centers in the (100)-cut anvil exhibit a drastic reduction in contrast with increasing pressure. The dominant culet stresses have symmetry-preserving and breaking projections on all NV subgroups, thereby inducing both a blue shift, Π_z , and a splitting, $2\Pi_{\perp}$ in the ODMR peaks. Notably, a surprising inversion of contrast is observed on the left peak around 60 GPa, as shown in the inset.

stress environment.

In this Letter, we combine an extensive set of first principles calculations with high-pressure NV experiments on three different culet orientations [i.e. (100)-, (110)- and (111)-oriented anvils]. Our *ab initio* simulations allow us to estimate two crucial sets of NV parameters as a function of the stress tensor: (i) the rates of inter-system crossing (ISC), which is a non-radiative transition between electronic states with different spin multiplicities and (ii) the spin polarization in the ground-state manifold. This enables us to propose and analyze a microscopic model that characterizes the NV’s optically-detected magnetic resonance (ODMR) contrast under general stress conditions. Our main results are two fold. For stress environments which pre-

serve the C_{3v} symmetry of the NV center, we predict that the optical contrast is mainly determined by the “upper” inter-system crossing rate, Γ_{ave} [Fig. 2(a)]. To test these predictions, we directly compare to DAC measurements exhibiting a range of different hydrostaticities [Fig. 3(b)] [10–13]. For symmetry-breaking stresses, we uncover a subtle interplay between the stress-induced spin-orbit coupling (SOC) and the Jahn-Teller (JT) effects of the NV center. This interplay causes a non-monotonic response of the NV center’s “lower” ISC rate, Γ_z^{lower} [Fig. 2(b)] as a function of stress (Fig. 4), and ultimately produces an unconventional polarization mechanism that yields the observed contrast inversion. While our *ab initio* simulations focus on the (100)-oriented culet, our proposed mechanism for contrast inversion should also apply to both (110)- and (111)-oriented culets. To this end, we perform experiments on both of these anvil cell geometries and indeed observe the predicted contrast inversion (Fig. 5).

Microscopics of the NV’s ODMR contrast—Each NV center hosts a spin-1 electronic ground state that can be optically polarized and read out [30, 31]. Here, we will work in the spin triplet basis $|m_s = 0, +, -\rangle$, where $|m_s = \pm\rangle = \frac{1}{\sqrt{2}}(|+1\rangle \pm |-1\rangle)$ and $|\pm 1\rangle$ are the familiar Zeeman eigenstates (where the quantization axis is defined along the NV axis).

NV center metrology is primarily performed via ODMR spectroscopy, where a 532-nm laser first excites the NV center and polarizes its population into the $|m_s = 0\rangle$ spin sublevel [30–32]. Microscopically, this polarization arises because the $|m_s = 0\rangle$ sublevels in 3E are forbidden to inter-system cross (into the 1A_1 manifold) at leading order [33, 34], while the lower inter-system crossing rates (Γ^{lower} , Fig. 2) exhibit a weak spin dependence [35]. Thus, during each optical cycle, population is preferentially transferred into the $|m_s = 0\rangle$ ground state; this yields the conventional experimental observation of $\gtrsim 70\%$ spin polarization [36, 37].

Crucially, the same optical pathway also naturally leads to spin-dependent fluorescence, enabling optical readout of the NV’s magnetic resonance spectra. In particular, since the $|m_s = 0\rangle$ sublevels in 3E exhibit an extremely small upper inter-system crossing rate, their dominant dynamics correspond to radiative relaxation directly to the ground state; since the laser excitation is spin-preserving, this immediately implies that the $|m_s = 0\rangle$ ground state is ‘brighter’ than the $|m_s = +, -\rangle$ states. ODMR spectroscopy proceeds by measuring the magnitude of the NV’s fluorescence dip (i.e. contrast) when a microwave field resonant with the spin transition is applied (compared to when it is off). To this end, the NV center’s contrast is controlled by two key ingredients, both determined by the ISC rates (Fig. 2): (i) the degree of spin polarization and (ii) the relative

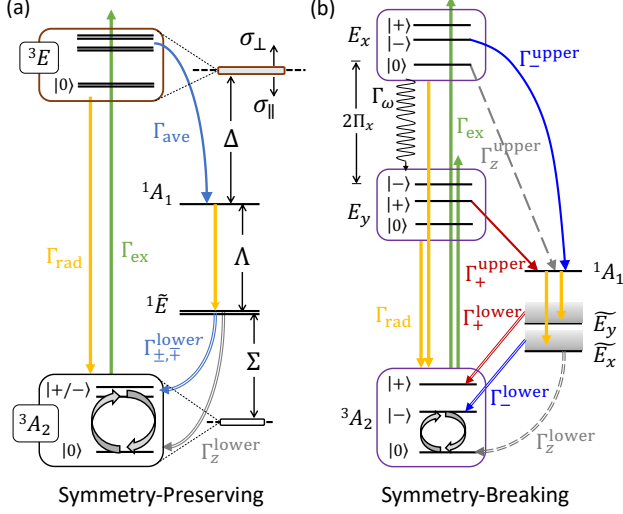


Figure 2. The negatively charged NV center’s energy level diagram and its optical cycle under (a) symmetry-preserving and (b) symmetry-breaking stress (here Π_x stress, defined in Supplemental Materials). The NV center’s low-lying electronic states contain two spin triplets 3A_2 and 3E , and two spin singlets 1A_1 and 1E , with three energy gaps defined as Δ, Λ, Σ in (a). The spin-1 basis adopted here is $|m_s = 0\rangle$, and $|m_s = \pm\rangle = \frac{1}{\sqrt{2}}(|m_s = 1\rangle \pm |m_s = -1\rangle)$, which are the spin eigenstates under Π_x stress. Notably, for symmetry-preserving stress, $\sigma_{\perp} = \frac{1}{2}(\sigma_{xx} + \sigma_{yy})$ and $\sigma_{\parallel} = \sigma_{zz}$ play qualitatively different roles in shifting energy gaps. Symmetry-breaking stress, however, breaks the defect’s point group symmetry and allows every spin state to participate in the optical cycle. The ISC rates are color coded for their spins, with blue, dark red, and grey for $|m_s = -, +, 0\rangle$, respectively in (b). The line styles denote the microscopic origin for these ISCs (see Supplemental Materials for details).

brightness of the three spin sublevels.

We evaluate the upper ISC rates using Fermi’s Golden rule [34], i.e., $\Gamma = \frac{2\pi}{\hbar} |\lambda|^2 F(\Delta)$, where the matrix element, $\lambda = \langle \psi_{\text{final}} | H_{\text{so}} | \psi_{\text{init}} \rangle$, arises from spin-orbit interactions and the vibrational overlap function $F(\Delta)$ characterizes the density of states at the gap Δ [Fig. 2(a)]. By comparison, the lower ISC rates are significantly more complicated, since they are forbidden at first order. In addition, 1E exhibits non-negligible electron-phonon coupling due to Jahn-Teller effects [35, 38]. Thus, we estimate the lower ISC rates by first solving for the vibronic wavefunction of the singlet states, i.e., $|\widetilde{{}^1E}\rangle, |\widetilde{{}^1A_1}\rangle$ from a Jahn-Teller model Hamiltonian [35, 38], and then evaluating their spin-orbit matrix elements and vibrational density of states with respect to 3A_2 (see Supplemental Materials for additional details).

Optimizing NV contrast for symmetry-preserving

stresses—We investigate a general symmetry-preserving stress of the form:

$$\sigma = \alpha \sigma_{\text{hyd}} + (1 - \alpha) \sigma_{[111]}, \quad (1)$$

where α characterizes the degree of hydrostaticity, and $\sigma_{\text{hyd}}, \sigma_{[111]}$ represent the hydrostatic and uniaxial [111] stresses, respectively. Since the symmetry of the NV center is preserved, the optical cycle is qualitatively the same as the ambient case.

To estimate the inter-system crossing rates, we compute the transverse SOC λ_{\perp} and $F(\Delta)$ [Fig. 3(a)] as a function of strain (and then convert to stress), for both the uniaxial [111] and hydrostatic cases (i.e. $\alpha = 0, 1$ respectively). A few remarks are in order. First, λ_{\perp} (red) increases with compression in both hydrostatic and uniaxial [111] environments, although the effect is significantly stronger for the former. Second, we find that $F(\Delta)$ (grey) exhibits opposite trends for the two types of stress environments, implying that the vibrational overlap increases significantly with uniaxial [111] strain, but is suppressed by hydrostatic strain [39].

Using λ_{\perp} and $F(\Delta)$, we now compute the upper ISC rates, Γ_{ave} , versus stress [dashed curves, Fig. 3(b)]. For hydrostatic stress (dark purple, $\alpha = 1$), the ISC rate exhibits a non-trivial trend, with a peak value at approximately ~ 30 GPa. Interestingly, this is a manifestation of competition between the behaviors of λ_{\perp} and $F(\Delta)$, where the former dominates at small stresses while the latter controls the large stress limit. For smaller α (i.e. a larger uniaxial component), Γ_{ave} exhibits a more monotonic behavior as a function of stress.

In order to predict how the NV’s ODMR contrast changes versus stress, we directly solve the rate-equation model for the NV’s optical cycle [Fig. 2(a)] utilizing these computed ISC rates. As depicted in Fig. 3(b) (solid curves), we find that uniaxial [111] stress ($\alpha = 0$), although not achievable in the conventional DAC setup, yields the largest NV contrast [40] and that there exists a strong correlation between the upper ISC rates (dashed curves) and the predicted contrast (solid curves).

To investigate these predictions, we directly measure [111]-NV contrast [extracted from Rabi oscillations, Fig. 3(d)] as a function of pressure in a (111)-cut diamond with NV centers implanted ~ 50 nm below the culet surface [Fig. 3(c)]. By carefully measuring the stress tensor at each pressure, we estimate the degree of hydrostaticity to be $\alpha \approx 0.73$. In addition, we also compare our predictions to two other sets of experimental NV-DAC measurements with differing degrees of hydrostaticity: (i) a nearly hydrostatic ($\alpha \approx 1$) measurement using NV’s contained within a nanopillar fabricated at the center of (100)-cut DAC [11], and (ii) a measurement with $\alpha \approx 0.57$ [13] that also utilizes NVs in a (111)-

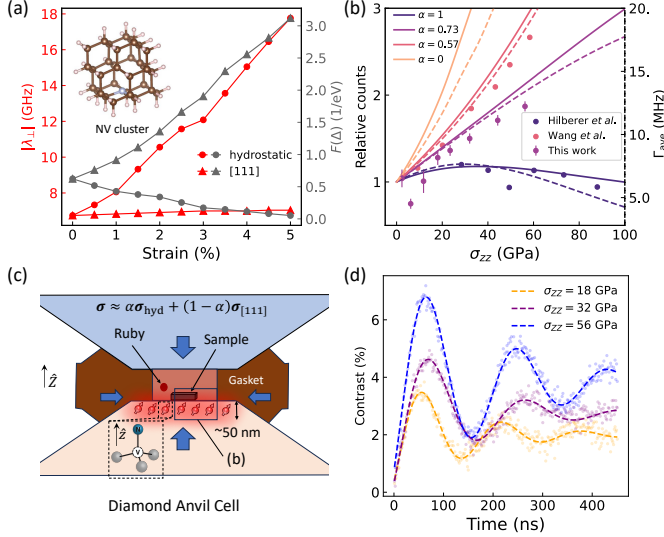


Figure 3. (a) Computations of the intermediate components of the upper ISC, i.e., transverse spin-orbit coupling λ_{\perp} (red) and vibrational overlap $F(\Delta)$ between the 3E and 1A_1 manifolds (gray) versus hydrostatic (circle) and uniaxial [111] strain (triangle). The inset shows a cluster model of the NV center, which we use as a basis for our *ab initio* calculations. (b) Upper ISC rate Γ_{ave} assembled from λ_{\perp} and $F(\Delta)$ (dashed), and comparison of the contrast (relative to that at the ambient condition) between simulation (solid) and experiments [11, 13] (dots), where the color codes the hydrostaticity α . Notably, the ISC rate exhibits a strong correlation with the relative contrast. (c) Schematic of a zoom-in DAC with (111)-cut diamond, and the embedded NV centers. (d) Rabi oscillations of the [111] NV at $\sigma_{zz} = 18, 32, 56$ GPa respectively, from which contrast is extracted. The experimental data are fitted by damped sine waves and plotted by the orange, purple and blue dashed lines.

cut DAC [41]. As illustrated in Fig. 3(c), all three sets of experimental measurements are in semi-quantitative agreement with our *ab initio* predictions. Interestingly, since our calculations consider only a single NV center, this suggests that the contrast enhancement from utilizing a (111)-cut anvil is *intrinsic* to the [111]-oriented NV itself, ruling out previous interpretations based on the ‘darkening’ of non-[111] NVs [13].

Microscopic origin of stress-induced positive NV contrast—Let us now turn to a second puzzle regarding the NV’s contrast in high-pressure experiments, namely, the observation of contrast inversion [depicted in Fig. 1(c) for a (100)-cut anvil] [42]. As previously discussed, conventional ‘negative’ contrast occurs because the NV becomes optically polarized to the ‘bright’ $|m_s = 0\rangle$ spin state, and the applied microwave transfers population into the comparatively ‘dark’ $|m_s = +, -\rangle$ states. Conversely, ‘positive’ contrast suggests that the NV is becoming polarized into a dark state. This hypothesis,

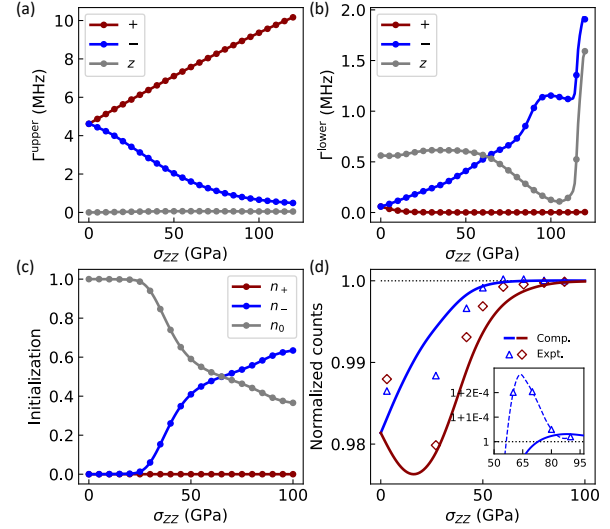


Figure 4. Computations of the ISC rates and ODMR contrast of NV centers in the (100)-cut diamond under stress. (a) Upper ISC rates versus stress with color codes for the three spins. (b) Lower ISC rates versus stress, with Γ_z^{lower} exhibiting non-monotonic trend coming from negative interference between different ISC mechanisms (see main text and SM). (c) Ground state population distribution among the three spins. A gradual transfer from n_0 to n_- begins around 25 GPa and n_- dominates the population from 65 GPa. (d) Simulated ODMR contrast (solid) obtained by solving the rate model defined in the main text, with ISC rates acting as inputs. Notably, the contrast inversion in the left peak (representing transitions $|m_s = 0\rangle \leftrightarrow |m_s = -\rangle$ driven by the MW) observed from experiments [12] (discrete) is reproduced, as shown in the inset. The ‘predicted’ onset of positive contrast is slightly later compared to experiments, and the magnitude is also smaller, with possible reasons for this discrepancy discussed in detail in the Supplemental Materials.

as we will see, requires the lower ISC to develop a strong spin selectivity towards population transfer into the dark states. Crucially, this selectivity is made possible by symmetry-breaking stresses, which open new ISC transitions within the NV’s optical cycle, e.g., $\Gamma_z^{\text{upper}}, \Gamma_z^{\text{lower}}$ [Fig. 2(b)].

To this end, let us begin by understanding the effect of symmetry-breaking stresses on the upper ISC rates. Under uniaxial [100] stress, the 3E sextuplet is split into two well-separated triplets, as the e orbital degeneracy is lifted [Fig. 2(b)]. Figure 4(a) depicts the upper ISC rates [defined in Fig. 2(b)] as a function of increasing [100] stress. The transition rate from $|m_s = +\rangle$ ($|m_s = -\rangle$) monotonically increases (decreases) with stress and is still primarily driven by the vibrational overlap between 3E_y (3E_x) and 1A_1 . This is because the 3E_x branch is rapidly detuned from 1A_1 (and vice versa for 3E_y). Meanwhile, the symmetry-

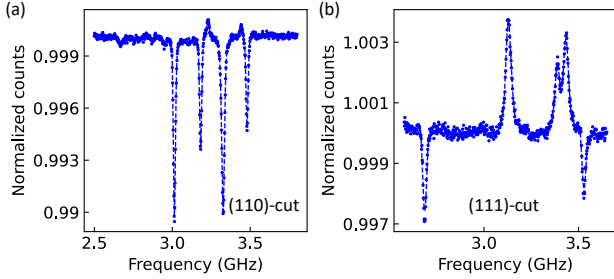


Figure 5. Positive contrast observed from ODMR measurements performed on NV centers in (a) (110)-cut anvil at 300 K, 25 GPa, $B_Z = 85$ G [7], and (b) (111)-cut anvil at 30 K, 28 GPa, $B_Z = 150$ G. For the latter, the positive contrast originates from the non-[111] NV centers.

breaking stress enables a non-zero Γ_z^{upper} , which connects $|m_s = 0\rangle$ to 1A_1 . Most importantly, we find that Γ_z^{upper} remains the smallest [Fig. 4(a)] throughout the entire pressure range investigated, confirming that the $|m_s = 0\rangle$ state remains the brightest.

Next, we turn to the fascinating case of the lower ISC. Much like 3E , the reduction of symmetry lifts the orbital degeneracy of 1E . Stress serves to progressively increase (decrease) the vibronic overlap between 1E_x (1E_y) and 3A_2 . In Fig. 4(b), we plot all three rates from the 1E singlet into the 3A_2 manifold. Among them, the behavior of Γ_z^{lower} is particularly intriguing owing to its non-monotonic behavior versus stress: It exhibits a significant drop-off beyond $\sigma_{ZZ} = 50$ GPa, and then increases sharply again after ~ 100 GPa. Somewhat remarkably, this results from the emergence of a new stress-induced spin-orbit channel from 1E_x , which *destructively interferes* with the existing Jahn-Teller-based channel (see Supplemental Materials). Above ~ 100 GPa, this new channel dominates, rapidly restoring the Γ_z^{lower} transition rate. Comparatively, Γ_z^{lower} progressively increases with stress and becomes dominant at $\sigma_{ZZ} \approx 60$ GPa, making the lower ISCs favor the dark spin state $|m_s = -\rangle$.

To this end, we observe a reversal of the spin selectivity of the lower ISC with symmetry breaking stress. By combining all of the aforementioned ISC rates, we compute the NV’s spin polarization [Fig. 4(c)] and fluorescence contrast [Fig. 4(d)]. For small stresses, the NV remains initialized to the $|m_s = 0\rangle$ state, while fraction initialized into the $|m_s = -\rangle$ state begins to increase at $\sigma_{ZZ} \sim 25$ GPa. At even larger stresses, $\sigma_{ZZ} \gtrsim 65$ GPa, the NV becomes dominantly polarized to the $|m_s = -\rangle$ state. This represents the complex interplay between several symmetry-breaking-stress-induced modifications to both the upper and lower ISCs. From the perspective of contrast, once the NV becomes initialized into the dark $|m_s = -\rangle$ state, the resulting ODMR spectrum

will naturally exhibit positive contrast [inset, Fig. 4(d)]. Interestingly, our theory predicts that while the ODMR peaks may exhibit contrast inversion, their positions still encode the same spectral content of the ground-state spin sublevel splittings.

Our theoretical framework also implies the existence of positive contrast in more general stress conditions. In particular, the interplay between symmetry breaking stresses and/or transverse magnetic fields can serve to hybridize excited state spin sublevels, enhancing the effective Γ_z^{upper} and thereby promoting ground state polarization inversion. To probe this generality, we perform high-pressure NV measurements in both a (110)-cut and a (111)-cut anvil. As shown in Fig. 5, in the presence of an external magnetic field, we observe contrast inversion for both settings.

Conclusion and Outlook—Our work opens the door to a number of intriguing future directions. First, our computational framework can readily be generalized to accommodate a wide array of environmental conditions, e.g. temperatures, electrical/magnetic fields, and stress environments. Moreover, our method can also be adapted to the vast emerging landscape of solid state spin defects [43–46], and will help identify candidates that are viable under extreme conditions. Second, while we have provided a general framework for the emergence of contrast inversion, the details of how and when such inversion occurs in different anvil cuts remains an open challenge. Third, we motivate the deliberate engineering of stress environments to promote metrological sensitivity. Our model suggests that achieving $\alpha = 0$ maximizes contrast. This stress environment may be obtained with a uniaxial press [47]. Meanwhile, a recent study makes use of NV center contrast inversion to perform measurements of the full stress tensor up to tens of GPa [19]. Finally, the phenomenon of positive contrast suggests the use of symmetry-breaking stresses as another tuning parameter for defect physics. Modifying the polarization dynamics of the NV center and other spin defects may prove useful in the context of both quantum information and quantum sensing.

Note Added—During the completion of this work, a related manuscript appeared [48], which explores the contrast inversion of the NV center under pressure in a (111)-cut anvil. The authors also conclude that this inversion arises from a reversal in spin polarization.

Acknowledgements—We gratefully acknowledge discussions with R. Jeanloz, T. Smart, and D. Budker. This work was supported in part by the Next Generation Quantum Science and Engineering (Q-NEXT) center that develops quantum science and engineering technologies, and by the Brown Institute for Basic Sciences. Q-NEXT is supported by the U.S. Department of Energy, Office of Science, National Quantum Information

Science Research Centers. S.V.M. acknowledges support from the National Science Foundation Graduate Research Fellowship under Grant No. DGE-1752814. B.K. and M.B. acknowledge support from NSF QLCI program (grant no. OMA-2016245). C.Z. acknowledges the support from Enterprise Science Fund of Intellectual Ventures Management, LLC. The computations performed in this research used resources from the University of Chicago Research Computing Center.

* These authors contributed equally to this work.

† nyao@fas.harvard.edu

‡ gagalli@uchicago.edu

- [1] A. Drozdov, P. Kong, V. Minkov, S. Besedin, M. Kuzovnikov, S. Mozaffari, L. Balicas, F. F. Balakirev, D. Graf, V. Prakapenka, *et al.*, Superconductivity at 250 k in lanthanum hydride under high pressures, *Nature* **569**, 528 (2019).
- [2] V. I. Levitas, High pressure phase transformations revisited, *Journal of Physics: Condensed Matter* **30**, 163001 (2018).
- [3] A. Jayaraman, Diamond anvil cell and high-pressure physical investigations, *Reviews of Modern Physics* **55**, 65 (1983).
- [4] M. Ishizuka, M. Iketani, and S. Endo, Pressure effect on superconductivity of vanadium at megabar pressures, *Physical Review B* **61**, R3823 (2000).
- [5] E. Gregoryanz, V. V. Struzhkin, R. J. Hemley, M. I. Erements, H.-k. Mao, and Y. A. Timofeev, Superconductivity in the chalcogens up to multimegabar pressures, *Physical Review B* **65**, 064504 (2002).
- [6] D. Jackson, C. Aracne-Ruddle, V. Malba, S. Weir, S. Catledge, and Y. Vohra, Magnetic susceptibility measurements at high pressure using designer diamond anvils, *Review of scientific instruments* **74**, 2467 (2003).
- [7] S. Hsieh, P. Bhattacharyya, C. Zu, T. Mittiga, T. J. Smart, F. Machado, B. Kobrin, T. O. Höhn, N. Z. Rui, M. Kamrani, S. Chatterjee, S. Choi, M. Zaletel, V. V. Struzhkin, J. E. Moore, V. I. Levitas, R. Jeanloz, and N. Y. Yao, Imaging stress and magnetism at high pressures using a nanoscale quantum sensor, *Science* **366**, 1349 (2019).
- [8] K. Y. Yip, K. O. Ho, K. Y. Yu, Y. Chen, W. Zhang, S. Kasahara, Y. Mizukami, T. Shibauchi, Y. Matsuda, S. K. Goh, *et al.*, Measuring magnetic field texture in correlated electron systems under extreme conditions, *Science* **366**, 1355 (2019).
- [9] M. Lesik, T. Plisson, L. Toraille, J. Renaud, F. Ocelli, M. Schmidt, O. Salord, A. Delobbe, T. Debuisschert, L. Rondin, *et al.*, Magnetic measurements on micrometer-sized samples under high pressure using designed nv centers, *Science* **366**, 1359 (2019).
- [10] J.-H. Dai, Y.-X. Shang, Y.-H. Yu, Y. Xu, H. Yu, F. Hong, X.-H. Yu, X.-Y. Pan, and G.-Q. Liu, Optically detected magnetic resonance of diamond nitrogen-vacancy centers under megabar pressures, *Chinese Physics Letters* **39**, 117601 (2022).
- [11] A. Hilberer, L. Toraille, C. Dailedouze, M.-P. Adam, L. Hanlon, G. Weck, M. Schmidt, P. Loubeyre, and J.-F. Roch, Enabling quantum sensing under extreme pressure: Nitrogen-vacancy magnetometry up to 130 gpa, *Physical Review B* **107**, L220102 (2023).
- [12] P. Bhattacharyya, W. Chen, X. Huang, S. Chatterjee, B. Huang, B. Kobrin, Y. Lyu, T. Smart, M. Block, E. Wang, *et al.*, Imaging the meissner effect in hydride superconductors using quantum sensors, *Nature* **627**, 73 (2024).
- [13] M. Wang, Y. Wang, Z. Liu, G. Xu, B. Yang, P. Yu, H. Sun, X. Ye, J. Zhou, A. F. Goncharov, *et al.*, Imaging magnetic transition of magnetite to megabar pressures using quantum sensors in diamond anvil cell, *Nature Communications* **15**, 8843 (2024).
- [14] D. Mai, C. Zhong, Z. Wang, H. Wang, X. Sun, R. Dai, Z. Wang, and Z. Zhang, Megabar pressure sensing and magnetic phase imaging by [111]-oriented nitrogen-vacancy centers in diamond, *Journal of Applied Physics* **138**, 10.1063/5.0278258 (2025).
- [15] Q. Hao, Z.-X. He, N. Zuo, Y. Chen, X. Xing, X. Zhang, X. Zhuang, Z. Shi, X. Chen, J.-G. Guo, *et al.*, Diamond quantum sensing at record high pressure up to 240 gpa, arXiv preprint arXiv:2510.26605 (2025).
- [16] C. Zhong, Y. Wang, D. Mai, C. Ye, X. Li, H. Wang, R. Dai, Z. Wang, X. Sun, and Z. Zhang, High spatial resolution 2d imaging of current density and pressure for graphene devices under high pressure using nitrogen-vacancy centers in diamond, *Nano Letters* **24**, 4993 (2024).
- [17] Y. Song, C. Ma, H. Wang, M. Zhou, Y. Qi, W. Cao, S. Li, H. Liu, G. Liu, and Y. Ma, Room-temperature superconductivity at 298 k in ternary lsc-h system at high-pressure conditions, arXiv preprint arXiv:2510.01273 (2025).
- [18] Y. Chen, J. Wen, Z.-X. He, J.-W. Fan, X.-Y. Pan, C. Ji, H. Gou, X. Yu, L. Chen, and G.-Q. Liu, Imaging magnetic flux trapping in lanthanum hydride using diamond quantum sensors, arXiv preprint arXiv:2510.21877 (2025).
- [19] S. V. Mandyam, E. Wang, Z. Wang, B. Chen, N. C. Jayarama, A. Gupta, E. A. Riesel, V. I. Levitas, C. R. Laumann, and N. Y. Yao, Uncovering origins of heterogeneous superconductivity in $\text{La}_3\text{Ni}_2\text{O}_7$ using quantum sensors, arXiv preprint arXiv:2510.02429 10.48550/arXiv.2510.02429 (2025).
- [20] L. Liu, J. Guo, D. Hu, G. Yan, Y. Chen, L. Yu, M. Wang, X.-D. Liu, and X. Huang, Evidence for the meissner effect in the nickelate superconductor $\text{La}_3\text{Ni}_2\text{O}_{7-\delta}$ single crystal using diamond quantum sensors, *Physical Review Letters* **135**, 096001 (2025).
- [21] A. Batalov, V. Jacques, F. Kaiser, P. Siyushev, P. Neumann, L. J. Rogers, R. L. McMurtree, N. B. Manson, F. Jelezko, and J. Wrachtrup, Low temperature studies of the excited-state structure of negatively charged nitrogen-vacancy color centers in diamond, *Physical Review Letters* **102**, 195506 (2009).
- [22] J. P. Tetienne, L. Rondin, P. Spinicelli, M. Chipaux, T. Debuisschert, J.-F. Roch, and V. Jacques, Magnetic-field-dependent photodynamics of single nv defects in diamond: an application to qualitative all-optical magnetic imaging, *New Journal of Physics* **14**, 103033

- (2012).
- [23] S. Ernst, P. J. Scheidegger, S. Diesch, and C. L. Degen, Modeling temperature-dependent population dynamics in the excited state of the nitrogen-vacancy center in diamond, *Physical Review B* **108**, 085203 (2023).
- [24] S. Ernst, P. J. Scheidegger, S. Diesch, L. Lorenzelli, and C. L. Degen, Temperature dependence of photoluminescence intensity and spin contrast in nitrogen-vacancy centers, *Physical Review Letters* **131**, 086903 (2023).
- [25] L. Rondin, J.-P. Tetienne, T. Hingant, J.-F. Roch, P. Maletinsky, and V. Jacques, Magnetometry with nitrogen-vacancy defects in diamond, *Reports on progress in physics* **77**, 056503 (2014).
- [26] D. A. Broadway, B. Johnson, M. Barson, S. E. Lillie, N. Donschuk, D. McCloskey, A. Tsai, T. Teraji, D. Simpson, A. Stacey, *et al.*, Microscopic imaging of the stress tensor in diamond using in situ quantum sensors, *Nano Letters* **19**, 4543 (2019).
- [27] K. O. Ho, K. C. Wong, M. Y. Leung, Y. Y. Pang, W. K. Leung, K. Y. Yip, W. Zhang, J. Xie, S. K. Goh, and S. Yang, Recent developments of quantum sensing under pressurized environment using the nitrogen vacancy (NV) center in diamond, *Journal of Applied Physics* **129**, 10.1063/5.0052233 (2021).
- [28] P. Kehayias, M. Turner, R. Trubko, J. Schloss, C. Hart, M. Wesson, D. Glenn, and R. Walsworth, Imaging crystal stress in diamond using ensembles of nitrogen-vacancy centers, *Physical Review B* **100**, 174103 (2019).
- [29] R. Suda, K. Uriu, K. Yamamoto, M. Sasaki, K. Sasaki, M. Einaga, K. Shimizu, and K. Kobayashi, Gpa pressure imaging using nanodiamond quantum sensors, *Journal of the Physical Society of Japan* **94**, 124707 (2025).
- [30] J. R. Maze, A. Gali, E. Togan, Y. Chu, A. Trifonov, E. Kaxiras, and M. D. Lukin, Properties of nitrogen-vacancy centers in diamond: the group theoretic approach, *New Journal of Physics* **13**, 025025 (2011).
- [31] M. W. Doherty, N. B. Manson, P. Delaney, and L. C. Hollenberg, The negatively charged nitrogen-vacancy centre in diamond: the electronic solution, *New Journal of Physics* **13**, 025019 (2011).
- [32] L. Robledo, H. Bernien, T. Van Der Sar, and R. Hanson, Spin dynamics in the optical cycle of single nitrogen-vacancy centres in diamond, *New Journal of Physics* **13**, 025013 (2011).
- [33] M. L. Goldman, A. Sipahigil, M. Doherty, N. Y. Yao, S. Bennett, M. Markham, D. Twitchen, N. Manson, A. Kubanek, and M. D. Lukin, Phonon-induced population dynamics and intersystem crossing in nitrogen-vacancy centers, *Physical Review Letters* **114**, 145502 (2015).
- [34] M. L. Goldman, M. Doherty, A. Sipahigil, N. Y. Yao, S. Bennett, N. Manson, A. Kubanek, and M. D. Lukin, State-selective intersystem crossing in nitrogen-vacancy centers, *Physical Review B* **91**, 165201 (2015).
- [35] G. Thiering and A. Gali, Theory of the optical spin-polarization loop of the nitrogen-vacancy center in diamond, *Physical Review B* **98**, 085207 (2018).
- [36] G. Waldherr, J. Beck, M. Steiner, P. Neumann, A. Gali, T. Fraunheim, F. Jelezko, and J. Wrachtrup, Dark states of single nitrogen-vacancy centers in diamond unraveled by single shot nmr, *Physical Review Letters* **106**, 157601 (2011).
- [37] Y. Song, Y. Tian, Z. Hu, F. Zhou, T. Xing, D. Lu, B. Chen, Y. Wang, N. Xu, and J. Du, Pulse-width-induced polarization enhancement of optically pumped nv electron spin in diamond, *Photonics Research* **8**, 1289 (2020).
- [38] Y. Jin, M. Govoni, and G. Galli, Vibrationally resolved optical excitations of the nitrogen-vacancy center in diamond, *npj Computational Materials* **8**, 238 (2022).
- [39] We note that this result is in agreement with expectations for the effects of these strains on Δ [49].
- [40] Although the uniaxial [111] stress is predicted to exhibit the best contrast, we find $\alpha \in [0.0, 0.1]$ all yield very similar contrast.
- [41] We note that in practice, α can deviate from the theoretical value of 0.61 derived from a semi-infinite anvil [50] due to the uniaxial bias imposed by the compression being done along the Z axis, and that variations in α between experiments relates to the slightly different mechanical conditions of different experimental configurations (culet size, gasket thickness, etc).
- [42] It has also been reported that local electric field around the NV center plus near resonance ODMR measurement (resonant optical excitation at zero phonon line wavelength) could also lead to positive contrast at cryogenic temperatures ($\sim 5K$) [51, 52]. The positive contrast that we investigate in this work is from off-resonant ODMR spectroscopy and therefore has a completely different mechanism.
- [43] G. Wolfowicz, F. J. Heremans, C. P. Anderson, S. Kanai, H. Seo, A. Gali, G. Galli, and D. D. Awschalom, Quantum guidelines for solid-state spin defects, *Nature Reviews Materials* **6**, 906 (2021).
- [44] W. Lee, V. S. Liu, Z. Zhang, S. Kim, R. Gong, X. Du, K. Pham, T. Poirier, Z. Hao, J. H. Edgar, P. Kim, C. Zu, E. J. Davis, and N. Y. Yao, Intrinsic high-fidelity spin polarization of charged vacancies in hexagonal boron nitride, *Physical Review Letters* **134**, 096202 (2025).
- [45] G. He, R. Gong, Z. Wang, Z. Liu, J. Hong, T. Zhang, A. L. Riofrio, Z. Rehfuss, M. Chen, C. Yao, *et al.*, Probing stress and magnetism at high pressures with two-dimensional quantum sensors, *Nature Communications* **16**, 8162 (2025).
- [46] M. Mohseni, L. Razinkovas, V. Žalandauskas, G. m. H. Thiering, and A. Gali, Magneto-optical properties of group-iv vacancy centers in diamond upon hydrostatic pressure, *Physical Review B* **112**, 155201 (2025).
- [47] M. S. J. Barson, P. Peddibhotla, P. Overtchaiyapong, K. Ganesan, R. L. Taylor, M. Gebert, Z. Mielens, B. Koslowski, D. A. Simpson, L. P. McGuinness, J. McCallum, S. Prawer, S. Onoda, T. Ohshima, A. C. Bleszynski Jayich, F. Jelezko, N. B. Manson, and M. W. Doherty, Nanomechanical Sensing Using Spins in Diamond, *Nano Letters* **17**, 1496 (2017).
- [48] Z. Liu, J. Sun, G. Xu, B. Yang, Y. Guo, Y. Wang, C. Xin, H. Zuo, M. Wang, and Y. Wang, Strain-engineered nanoscale spin polarization reversal in diamond nitrogen-vacancy centers, *arXiv preprint arXiv:2511.05373* (2025).
- [49] G. Davies and M. Hamer, Optical studies of the 1.945 eV vibronic band in diamond, *Proceedings of the Royal Society of London. A. Mathematical and Physical Sciences* **348**, 285 (1976).

- [50] A. L. Ruoff, H. Luo, and Y. K. Vohra, The closing diamond anvil optical window in multimegabar research, *Journal of Applied Physics* **69**, 6413 (1991).
- [51] M. Block, B. Kobrin, A. Jarmola, S. Hsieh, C. Zu, N. Figueroa, V. Acosta, J. Minguzzi, J. Maze, D. Budker, and N. Yao, Optically enhanced electric field sensing using nitrogen-vacancy ensembles, *Physical Review Applied* **16**, 024024 (2021).
- [52] R. Akhmedzhanov, L. Gushchin, N. Nizov, V. Nizov, D. Sobgayda, I. Zelensky, and P. Hemmer, Optically detected magnetic resonance in negatively charged nitrogen-vacancy centers in diamond under resonant optical excitation at cryogenic temperatures, *Physical Review A* **94**, 063859 (2016).
- [53] B. O. Roos, The complete active space scf method in a fock-matrix-based super-ci formulation, *International Journal of Quantum Chemistry* **18**, 175 (1980).
- [54] P. Giannozzi, O. Basergio, P. Bonfà, D. Brunato, R. Car, I. Carnimeo, C. Cavazzoni, S. De Gironcoli, P. Delugas, F. Ferrari Ruffino, *et al.*, Quantum espresso toward the exascale, *The Journal of Chemical Physics* **152**, 10.1063/5.0005082 (2020).
- [55] C. Bhandari, A. L. Wysocki, S. E. Economou, P. Dev, and K. Park, Multiconfigurational study of the negatively charged nitrogen-vacancy center in diamond, *Physical Review B* **103**, 014115 (2021).
- [56] K. Li, V. D. Dergachev, I. D. Dergachev, S. Zhang, S. A. Varganov, and Y. Ping, Excited-state dynamics and optically detected magnetic resonance of solid-state spin defects from first principles, *Physical Review B* **110**, 184302 (2024).
- [57] Z. Benedek, Á. Ganyecz, A. Pershin, V. Ivády, and G. Barcza, Accurate and convergent energetics of color centers by wavefunction theory, *npj Computational Materials* **11**, 346 (2025).
- [58] F. Neese, F. Wennmohs, U. Becker, and C. Riplinger, The orca quantum chemistry program package, *The Journal of Chemical Physics* **152**, 10.1063/5.0004608 (2020).
- [59] Y. Jin, J. Park, M. M. McMillan, D. D. Ohm, C. Barnes, B. Pingault, C. Egerstrom, B. Huang, M. Govoni, F. J. Heremans, *et al.*, First-principles framework for the prediction of intersystem crossing rates in spin defects: The role of electron correlation, *Physical Review Letters* **135**, 036401 (2025).
- [60] S. Chen, V. W.-z. Yu, Y. Jin, M. Govoni, and G. Galli, Advances in quantum defect embedding theory, *Journal of Chemical Theory and Computation* 10.1021/acs.jctc.5c00559 (2025).
- [61] L. Otis, Y. Jin, V. W.-z. Yu, S. Chen, L. Gagliardi, and G. Galli, Strongly correlated states of transition metal spin defects: the case of an iron impurity in aluminum nitride, *The Journal of Physical Chemistry Letters* **16**, 3092 (2025).
- [62] V. Somjit, J. Davidsson, Y. Jin, and G. Galli, An nv-center in magnesium oxide as a spin qubit for hybrid quantum technologies, *npj Computational Materials* **11**, 74 (2025).

END MATTER

The pursuit of accurate and efficient methods for solving the electronic structure problem has been the holy grail of computational chemistry and condensed matter physics. One central physical quantity investigated in this work is the spin orbit coupling (SOC), which is numerically obtained using the complete active space self-consistent field (CASSCF) method [53] applied to a single-NV cluster [54, 55], as shown in the inset of Fig. 3(a). This model has been widely adopted in several recent studies [55–57] due to its affordable computational cost and availability of codes [58].

During this research, a subset of the authors developed an alternative description [59] of the defect’s SOC based on a quantum defect embedding theory (QDET) [60] which partitions the problem into separate calculations of the defect center and of the host material. Since this approach uses periodically repeated cells, the surrounding solid-state environment is represented more accurately. QDET is based on a Green’s function formalism, and has been applied to study several defects in semiconductors [61, 62] for quantum technologies. In this End Matter, we shall make a comparison of these two computational approaches, showcasing their respec-

tive pros and cons, to guide future computational or applied research.

In Table. S6 in the Supplemental Materials, we compare the upper ISC rates computed from these two methods with experimental measurements in ambient conditions, showing that the QDET approach [59] gives a better agreement with experiment, while the CASSCF@cluster approach gives results roughly one order of magnitude smaller than what is observed. The inaccuracy of the CASSCF approach can be traced back to an underestimation of λ_{\perp} (see Table. S4). By comparing the weights of different configurations in the many-body wavefunctions from Ref. [56] and Ref. [59], we expect that this underestimation arises from the relatively large weight ($\sim 20\%$) of the $e_x^2 e_y^2$ configuration in the 1A_1 wavefunction from CASSCF (see Sec. S6.2 in the Supplemental Materials for details). However, in this work, the relevant quantities in our calculations are the strain/stress susceptibilities of SOCs, and CASSCF@cluster provides a consistent way to estimate them, as we reach a semi-quantitative agreement with experimental ODMR measurements.

Future work will employ the QDET approach to refine the estimation of susceptibilities.